

IP Eri: A surprising long-period binary system hosting a He white dwarf

T. Merle¹, A. Jorissen¹, T. Masseron¹, S. Van Eck¹, L. Siess¹, and H. Van Winckel²

¹ Institut d'Astronomie et d'Astrophysique, Université Libre de Bruxelles, CP. 226, Boulevard du Triomphe, 1050 Brussels, Belgium
e-mail: tmerle@ulb.ac.be

² Instituut voor Sterrenkunde, Katholieke Universiteit Leuven, Celestijnenlaan 200D, 3200 Heverlee, Belgium

Received ...; accepted ...

ABSTRACT

We determine the orbital elements for the K0 IV + white dwarf (WD) system IP Eri, which appears to have a surprisingly long period of 1071 d and a significant eccentricity of 0.25. Previous spectroscopic analyses of the WD, based on a distance of 101 pc inferred from its Hipparcos parallax, yielded a mass of only $0.43 M_{\odot}$, implying it to be a helium-core WD. The orbital properties of IP Eri are similar to those of the newly discovered long-period subdwarf B star (sdB) binaries, which involve stars with He-burning cores surrounded by extremely thin H envelopes, and are therefore close relatives to He WDs. We performed a spectroscopic analysis of high-resolution spectra from the HERMES/Mercator spectrograph and concluded that the atmospheric parameters of the K0 component are $T_{\text{eff}} = 4960$ K, $\log g = 3.3$, $[\text{Fe}/\text{H}] = 0.09$ and $\xi = 1.5 \text{ km s}^{-1}$. The detailed abundance analysis focuses on C, N, O abundances, carbon isotopic ratio, light (Na, Mg, Al, Si, Ca, Ti) and *s*-process (Sr, Y, Zr, Ba, La, Ce, Nd) elements. We conclude that IP Eri abundances agree with those of normal field stars of the same metallicity. The long period and non-null eccentricity indicate that this system cannot be the end product of a common-envelope phase; it calls instead for another less catastrophic binary-evolution channel presented in detail in a companion paper.

Key words. Stars: abundances – binaries: spectroscopic – Stars: evolution – Stars: individual: IP Eri – subdwarfs – white dwarfs

1. Introduction

IP Eri is a very interesting system consisting of a K0 (sub)giant and a He white dwarf (WD) and it is tempting to relate this system to the family of subdwarf B (sdB) binaries where the hot component is a bare He-burning core surrounded by an extremely thin H envelope (Heber 2009). These systems owe their properties to envelope ejection, likely due to binary interaction, as they evolve along the red giant branch. Their evolution shares some similarities with that of IP Eri and such systems are important benchmarks for binary evolution.

Several long-period eccentric systems (with $P \sim 10^3$ d) were recently discovered among sdB stars (Østensen & Van Winckel 2011, 2012; Vos et al. 2012, 2013; Deca et al. 2012; Barlow et al. 2012, 2013). Using new radial-velocity data collected with the HERMES/Mercator spectrograph (Raskin et al. 2011), we show in this paper (Sect. 3) that IP Eri adds to this new class of long-period eccentric systems.

Since the He-WD progenitor did not evolve along the asymptotic giant branch (AGB), it had no chance to produce *s*-process elements and to pollute its companion (the present K0 subgiant), so that the latter should not appear as a barium star (a family of K giants with enhanced abundances of *s*-process elements; Bidelman & Keenan 1951). It is therefore of interest to perform a chemical analysis of the K0 subgiant in the IP Eri system to confirm the absence of overabundances of *s*-process elements. This is the second objective of the present paper, which is organized as follows: Sect. 2 gives an overview of the properties of the IP Eri system. Sect. 3 presents the radial-velocity data and the ensuing orbit. After deriving the atmospheric parameters of IP Eri in Sect. 4, the abundance analysis is presented in Sect. 5,

with emphasis on *s*-process elements. These abundances are then compared with expectations for barium stars and for non-*s*-process-polluted stars, as derived from the abundance trends observed in large samples of field stars reflecting the chemical evolution of the Galaxy (Sect. 6). Sect. 7 briefly confronts our results with predictions from binary-evolution scenarios presented in detail in a companion paper (Siess et al. 2014). Sect. 8 summarizes our results.

2. The IP Eri system

IP Eri (HD 18131, HIP 13558, WD 0252-055, EUVE J0254-053) has attracted attention since its discovery as an extreme UV (EUV) source both by *ROSAT* (Pounds et al. 1993; Pye et al. 1995) and *EUVE* (Bowyer et al. 1994; Malina et al. 1994; Bowyer et al. 1996). In a subsequent analysis, Vennes et al. (1995) find that an older *International Ultraviolet Explorer* (*IUE*) spectrum already revealed that a WD dominates the *IUE* spectrum below 200 nm while a K0 spectrum prevails at longer wavelengths. Their model-atmosphere analysis of the EUV photometry reveals a hot, hydrogen-rich (DA) WD (with an effective temperature of about 30 000 K) that is the most likely source of the EUV emission. In the grid of models fitted to the WD spectrum by Burleigh et al. (1997), the model with a temperature of 29 290 K, a gravity of $\log g = 7.5$ and a mass of $0.43 M_{\odot}$ locates the WD at a distance of 93 pc, consistent with the Hipparcos parallax of the K star, as discussed below. The corresponding age for the WD is then 7 Myr (Burleigh et al. 1997). The WD parameters inferred by Burleigh et al. (1997) locate it among He WDs in the $\log g - \log T_{\text{eff}}$ diagram of Driebe et al. (1998). Its mass of $0.43 M_{\odot}$ is incompatible with a CO WD since the min-

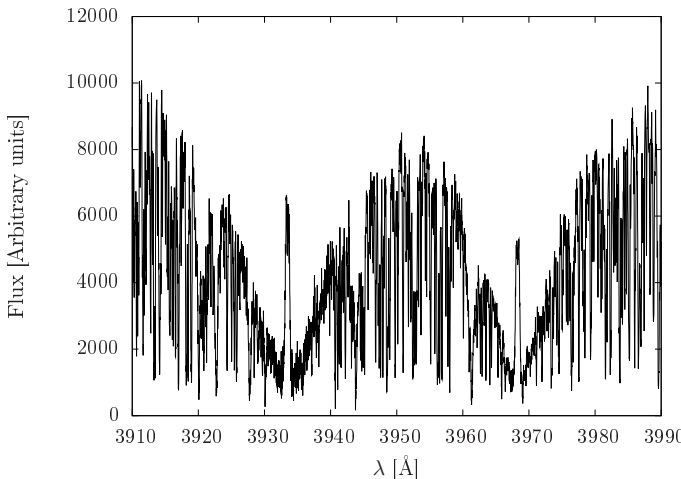


Fig. 1. The Ca II H and K lines, from the HERMES spectrum on HJD 2455066.748 (2009, August 23). The emission present in the cores is somewhat more intense than the one presented in Fig. 5 of Vennes et al. (1997).

imum CO core mass at the base of the AGB (just at the end of core He-burning) is $0.51 M_{\odot}$ (for a star of initial mass $0.9 M_{\odot}$; e.g., Eq. 66 of Hurley et al. 2000). An independent study by Vennes et al. (1998) concludes at a somewhat higher mass ($0.48 - 0.52 M_{\odot}$) for the IP Eri WD, which is still, for the most part of this range, compatible with the He nature of the WD.

The revised Hipparcos parallax of 9.82 ± 0.94 mas corresponds to a distance of 101 ± 11 pc and a distance modulus of 5.03 ± 0.2 (van Leeuwen 2007). With $V = 7.32$ (Cutispoto et al. 1995), one gets an absolute magnitude of 2.29 for the K star, which indicates that it is a subgiant. The photometric data for the K0 subgiant are $V = 7.32$, $U - B = 0.74$, $B - V = 0.98$, $V - Rc = 0.52$, $V - Ic = 0.97$ (Cutispoto et al. 1995) and $J = 5.709$, $H = 5.263$, $K = 5.090$ (2MASS; Cutri et al. 2003). The corresponding $V - K$ index of 2.23 implies an effective temperature of 4900 K (Bessell et al. 1998). Using a Bayesian method, Bailer-Jones (2011) obtains $\log T_{\text{eff}} = 3.70 \pm 0.01$ (5012 K) for IP Eri.

Although neither the ASAS lightcurve (Pojmanski 1997) nor the monitoring performed by Cutispoto et al. (1999) reveals variability at the 0.1 mag level, a more accurate monitoring by Strassmeier et al. (2000) has uncovered a 0.045 mag variability over 30 d in the Strömgren y band, hence its classification as a BY Dra variable in the General Catalogue of Variable Stars (with name IP Eri). The star is slowly rotating ($V \sin i < 5 \text{ km s}^{-1}$; Cutispoto et al. 1999). Should the 30 d photometric variability be due to rotation, a value of $\sim 1 \text{ km s}^{-1}$ for the rotational velocity would result from the radius of $3.8 R_{\odot}$ derived in (Siess et al. 2014) for IP Eri. Nevertheless, this star exhibits moderate Mg II h and k emission in the IUE spectrum and Ca II H & K emission (Fig. 5 of Vennes et al. 1997; Strassmeier et al. 2000). Fig. 1 shows the emission core in the Ca II lines, as seen on our HERMES/Mercator spectrum obtained on HJD 2455066.748 (2009, August 23). This emission core is somewhat more intense than the one presented by Vennes et al. (1997).

3. Orbital elements

The 18 high-resolution spectra used to compute the spectroscopic orbital elements were obtained with the HERMES/Mercator spectrograph (Raskin et al. 2011), operating at

Table 1. Radial velocities used for computing the orbit of the IP Eri system. Uncertainties on the radial velocities are about 40 m s^{-1} .

HJD	$V_r (\text{km s}^{-1})$
2455046.711	11.17
2455066.748	11.47
2455080.698	11.70
2455132.581	12.54
2455201.387	13.40
2455218.405	13.60
2455421.686	16.16
2455497.538	16.80
2455572.383	17.13
2455936.430	12.65
2455953.412	12.04
2455966.392	11.75
2455967.331	11.83
2456131.726	11.39
2456199.603	12.34
2456247.567	13.13
2456309.336	13.95
2456332.371	14.33

an average resolution of 85 000 in high-resolution mode and with a spectral range of $[\lambda 370 - 900 \text{ nm}]$. The spectra were reduced with the HERMES pipeline, and the radial velocities, computed by cross-correlating the observed spectra with an Arcturus template, are on the IAU wavelength system defined by the standards from Udry et al. (1999a,b). The individual radial velocities V_r are listed in Table 1. The errors are dominated by the drift of the air refractive index caused by the atmospheric pressure variations in the spectrograph room (see Fig. 9 in Raskin et al. 2011). The long-term stability during the 4 years of operations of the HERMES spectrograph turns out to be $\sim 40 \text{ m s}^{-1}$ as derived from the standard deviation of the radial velocities of the monitored IAU standards. This may be considered as the precision on the radial velocities produced by HERMES.

The corresponding orbital solution is listed in Table 2 and displayed in Fig. 2. The uncertainties of about 30 m s^{-1} on the orbital parameters V_y and K_1 are consistent with the precision of the spectrograph. Our orbital solution does not include the radial-velocity measurement $V_r = 14.94 \pm 0.10 \text{ km s}^{-1}$ obtained by Chubak et al. (2012) on JD 2 455 261, but we checked *a posteriori* that it falls on the orbital solution within 0.1 km s^{-1} . It is worth mentioning that IP Eri was imaged using the *HST* by Barstow et al. (2001) and the binary was not resolved, setting an upper limit on the orbital period of about 19 yr, consistent with the 2.9-yr period found here. No orbit could be adjusted to the O-C residuals of the IP Eri system (see lower panel of Fig. 2) when testing for the presence of a hypothetical third component.

The current mass function of the system $f(M_1, M_2) = 0.0036 M_{\odot}$ constrains the primary mass M_1 to be lower than $4.27 M_{\odot}$, if $M_2 = 0.43 M_{\odot}$ for the He-WD (see Sect. 2).

4. Atmospheric parameters

To derive the atmospheric parameters and the detailed abundances, we used two spectra with high signal-to-noise ratios from the list of Table 1 (namely those obtained on August

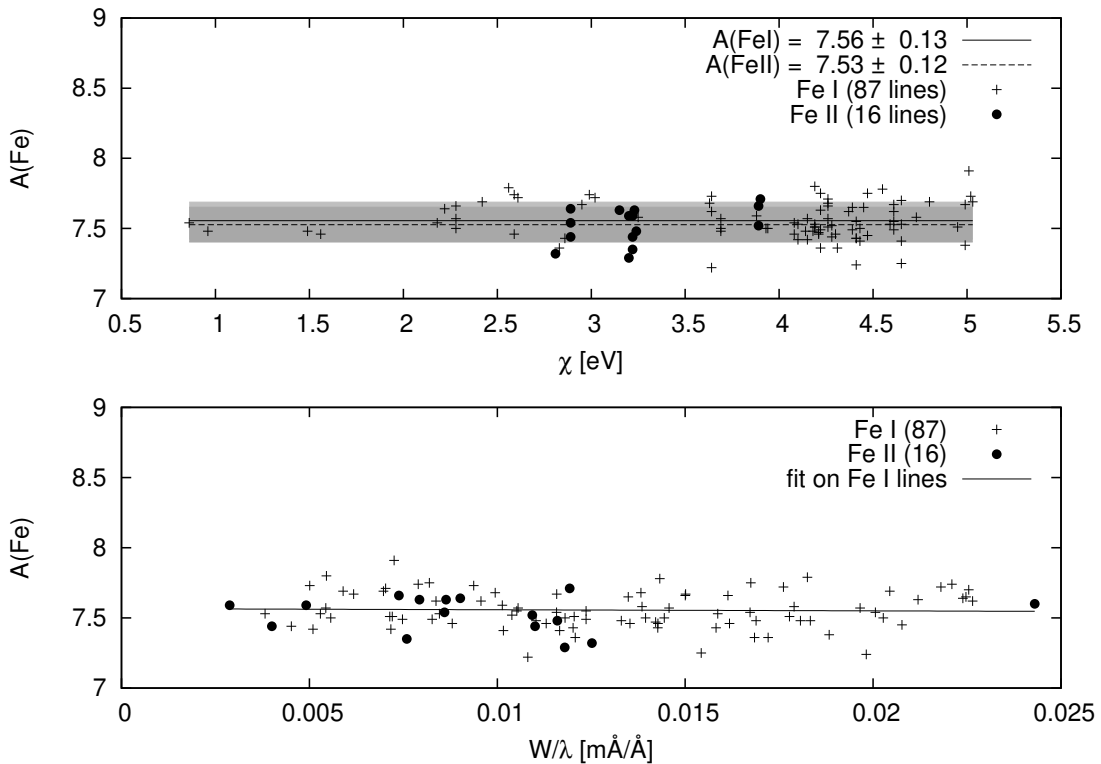


Fig. 3. Line by line abundance analysis for Fe I and Fe II lines as a function of the excitation potential χ and the reduced equivalent width W/λ . The grey areas represent the standard deviations around the mean abundances of Fe I and Fe II.

Table 2. Spectroscopic orbital elements of IP Eri.

ω ($^{\circ}$)	128.3	\pm	2.0
e	0.25	\pm	0.01
P (d)	1071.0	\pm	1.8
T_0 (JD)	2 455 956.9	\pm	4.7
V_γ (km s $^{-1}$)	+14.59	\pm	0.03
K_1 (km s $^{-1}$)	3.30	\pm	0.03
$f(M)$ (M_\odot)	0.0036	\pm	0.0001
$a_1 \sin i$ (Gm)	47.13		
N	18		
$\sigma(O-C)$ (km s $^{-1}$)	0.06		

22 and September 5, 2009, respectively HJD 2455066.748 and 2455080.698)¹. The first guesses for the atmospheric parameters were determined from the photometry. The color indices $J - K = 0.62$ and $V - K = 2.23$ yield a first estimate of $T_{\text{eff}} = 4900$ K for the effective temperature, using the calibrations of Bessell et al. (1998), in perfect agreement with previous estimates. From the calibration of MK spectral types provided by Cox (2000), we adopted $\log g = 2.1$ as initial guess for the surface gravity of a giant star of spectral type K0 (despite the fact that the luminosity class suggests a higher gravity). We initially assumed the metallicity to be solar.

The atmospheric parameters were then determined iteratively using the BACCHUS pipeline developed by one of the

¹ HERMES Spectra are available on electronic form at the CDS via anonymous ftp to cdsarc.u-strasbg.fr (130.79.128.5) or via <http://cdsweb.u-strasbg.fr/cgi-bin/qcat?J/A+A/>

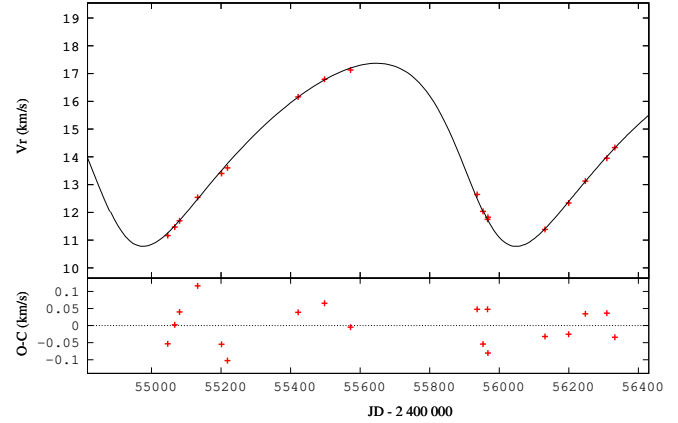


Fig. 2. The orbital solution for IP Eri. The lower panel shows the observed (O) minus the calculated (C) orbits.

author (TMA; see also Jofre et al. 2013) in the context of the Gaia-ESO survey (Gilmore et al. 2012). This pipeline is based on the 1D LTE spectrum-synthesis code Turbospectrum (Alvarez & Plez 1998; Plez 2012) and allows an automated determination of effective temperature T_{eff} , surface gravity $\log g$, metallicity $[\text{Fe}/\text{H}]$ and microturbulent velocity ξ . We used MARCS model atmospheres (Gustafsson et al. 2008) along with a selection of neutral and singly ionized Fe lines that have been selected for the analysis of stellar spectra in the framework of the Gaia-ESO survey. Oscillator strengths are from the VALD database (Kupka et al. 2000). The classical method to obtain the atmospheric parameters consists in avoiding trends in the $[\text{Fe}/\text{H}]$

Table 3. Results of the chemical abundance analysis. $A(X)$ is the abundance of species X in the logarithmic scale where $A(H) = 12$. σ_{stat} is the line-to-line abundance dispersion. N is the number of lines used for the corresponding species. In the column labelled 'comments', wavelengths are expressed in nm.

X		$A(X)$	[X/H]	[X/Fe]	σ_{stat}	N	comments
C	I	8.56	0.17	0.08	0.16	17	atomic lines
N	I	7.85	0.07	-0.02	-	1	$\lambda 868.34$
N		7.75	-0.03	-0.12	0.11	447	CN lines
O	I	8.82	0.16	0.07	-	1	$\lambda 630.03$
Na	I	6.45	0.28	0.19	0.11	8	
Mg	I	7.80	0.27	0.18	0.10	10	
Al	I	6.67	0.30	0.21	0.04	7	
Si	I	7.55	0.04	-0.05	0.10	15	
Ca	I	6.59	0.28	0.19	0.04	8	
Ti	I	5.14	0.24	0.15	0.15	9	
Ti	II	5.03	0.13	0.04	0.15	5	
Fe	I	7.56	0.11		0.13	87	
Fe	II	7.53	0.08		0.12	16	
Sr	I	3.10	0.18	0.09	0.04	3	
Y	I	2.33	0.12	0.03	0.05	2	$\lambda 619.17, \lambda 643.50$
Y	II	1.94	0.27	0.18	0.11	5	
Zr	I	2.89	0.31	0.22	0.18	4	
Zr	II	2.82	0.24	0.15	0.01	2	$\lambda 444.30, \lambda 535.01$
Ba	II	2.44	0.27	0.18	0.04	4	
La	II	1.17	0.04	-0.05	0.14	10	
Ce	II	1.57	-0.13	-0.22	0.08	4	
Nd	II	1.50	+0.05	-0.04	0.12	8	

vs. χ and [Fe/H] vs. W/λ relations (where χ is the lower excitation energy of the considered line, W its measured equivalent width and λ its wavelength) but also in forcing lines of Fe I and Fe II to yield the same abundance (see Fig. 3).

The equivalent widths are automatically measured using spectrum synthesis with the atmospheric parameters determined at the previous iteration. The synthetic spectra were convolved with a Gaussian function with full width at half maximum of 6.5 km s⁻¹. Only iron lines having reduced equivalent widths (W/λ) lower than 0.025 mÅ/Å were kept in the analysis. We thus obtain the following atmospheric parameters: $T_{\text{eff}} = 4960 \pm 100$ K, $\log g = 3.3 \pm 0.3$, $[\text{Fe}/\text{H}] = +0.09 \pm 0.08$ and $\xi = 1.5 \pm 0.1$ km s⁻¹. We used the solar reference values from Grevesse et al. (2007) where $A_{\odot}(\text{Fe}) = 7.45$.

5. Abundances

The detailed abundance analysis was performed (in the framework of Local Thermodynamical Equilibrium – LTE) using the abundance module of the BACCHUS pipeline. The selection of atomic and molecular lines was performed over the whole wavelength range covered by the HERMES/Mercator spectrograph. The atomic line list used for the detailed analysis is given in Appendix A. It includes the isotopic shifts for Ba II (with an update for isotopes 130 and 132) and the hyperfine structure for La II from Masseron (2006). The CH molecular line list is from Masseron et al. (2014). The references for the other molecular line lists (TiO, SiO, VO, C₂, CN, NH, OH, MgH, SiH, CaH and FeH) can be found in Gustafsson et al. (2008). Line fitting is essentially based on a least-square minimization method and all lines are visually inspected to check for possible bad fits (due to, e.g., line blends, cosmic hits, ...). The results of the detailed abundance analysis are presented in Table 3.

5.1. C, N, O and $^{12}\text{C} / ^{13}\text{C}$

The numerous neutral carbon atomic lines lead to an abundance of $[\text{C}/\text{Fe}] = 0.08 \pm 0.16$ dex. The nitrogen abundance is determined from one atomic line and from numerous molecular CN lines selected over a large spectral range [$\lambda 640 - 890$ nm]; atomic and molecular abundances agree within the statistical uncertainties. The only useful N I line ($\lambda 868.34$ nm) is weak ($W = 16$ mÅ) and in the red wing of a saturated Ti I line. An example of the fit of CN lines in the [$\lambda 812.2 - 813.2$ nm] region is shown in Fig. 4: synthetic spectra with $[\text{N}/\text{Fe}] = -0.12 \pm 0.3$ dex (see Table 3) are compared with the observed spectrum of IP Eri. The oxygen abundance is derived from the sole [O I] $\lambda 630.03$ nm line which is supposed to be free from NLTE effects (Asplund 2005). Another forbidden line at $\lambda 636.38$ nm is in the red wing of a Ca I autoionization line which is difficult to fit in our spectrum. The oxygen triplet at $\lambda 777.19, 777.42$ and 777.54 nm gives an abundance $A(\text{O}) \approx 9.46 \pm 0.07$ dex, in disagreement by about 0.7 dex with respect to the $\lambda 630.03$ nm line. This discrepancy is mainly due to the NLTE effect of diffusion in the triplet as clearly explained by Asplund (2005). No OH lines are available in the HERMES spectrum to better constrain the oxygen abundance. The resulting C/O ratio is 0.55, in agreement with the solar value.

The carbon isotopic ratio $^{12}\text{C} / ^{13}\text{C}$ is deduced from the ^{12}CN and ^{13}CN molecular lines in the [$\lambda 799.5 - 801.5$ nm] range (see, e.g., Barbuy et al. 1992; Drake & Pereira 2008). Specifically, we can compare the ^{12}CN triplet between $\lambda 800.3$ and $\lambda 800.4$ nm with the ^{13}CN feature at $\lambda 800.45$ nm, and the ^{12}CN weak line at $\lambda 801.0$ nm with the ^{13}CN very weak line at $\lambda 801.05$ nm. The latter is in the far red wing of the former. The high resolution of the HERMES spectrograph is able to separate the two components. The best fit of the entire [$\lambda 799.5 - 801.5$ nm] spectral range gives a carbon abundance of $A(\text{C}) = 8.56 \pm 0.10$ dex, which confirms the abundance derived from atomic carbon lines. With this value, we can only deduce a lower limit for the carbon isotopic ratio of $^{12}\text{C} / ^{13}\text{C} \geq 20$, in accordance with the weakness of the ^{13}CN features.

5.2. Light elements

Neutral lines from Na, Mg, Al, Si and Ca provide reliable abundances with a standard deviation lower than, or of the order of, 0.1 dex. Ca is the most enriched among the investigated α -elements, and has the lowest dispersion. The Ti abundance derived from Ti I lines is consistent with that of Mg and Ca, whereas the Ti abundance derived from Ti II is 0.1 dex lower but still within the statistical uncertainties. IP Eri is slightly enriched in α -elements ($[\alpha/\text{Fe}] = 0.17 \pm 0.06$ when considering Mg, Ca and Ti). The iron abundance determination is illustrated on Fig. 3 and is consistent with the derived metallicity.

5.3. s-process elements

Abundances for elements from the first two s-process peaks are measurable in IP Eri and their values are listed in Table 3. Examples of synthetic spectra are shown around two second-peak s-process elements (see Figs. 5 and 6) with solar ($[\text{Ba}, \text{Ce}/\text{Fe}] = 0.00$), enhanced ($[\text{Ba}, \text{Ce}/\text{Fe}] = 1.00$) and actual abundances ($[\text{Ba}/\text{Fe}] = 0.18$ and $[\text{Ce}/\text{Fe}] = -0.22$). For elements from the first s-process peak, lines of neutral and singly ionized Y and Zr are available. Abundances from neutral and ionized species agree within the statistical uncertainties, with abundances from neutral lines being somewhat lower than those

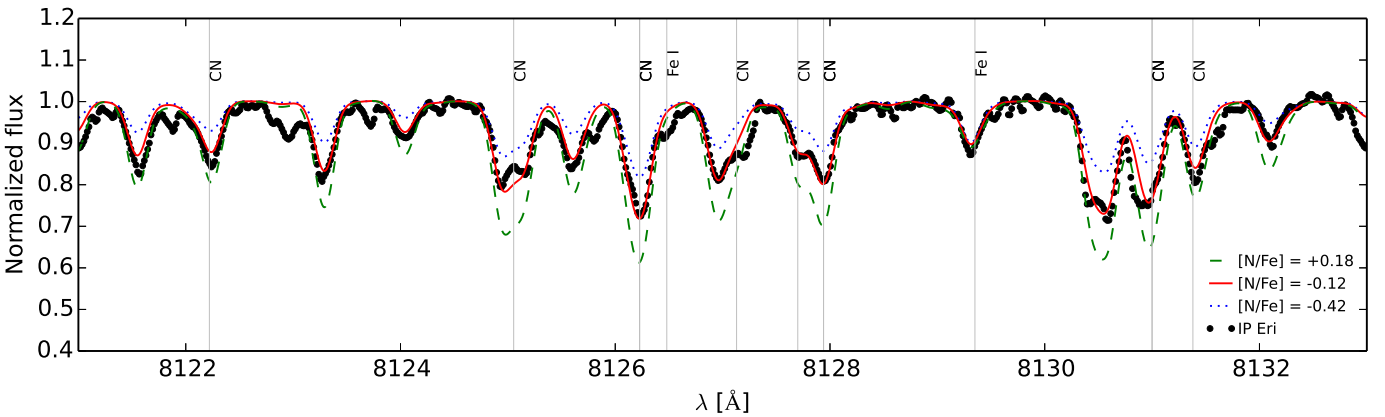


Fig. 4. Example of CN-line fitting.

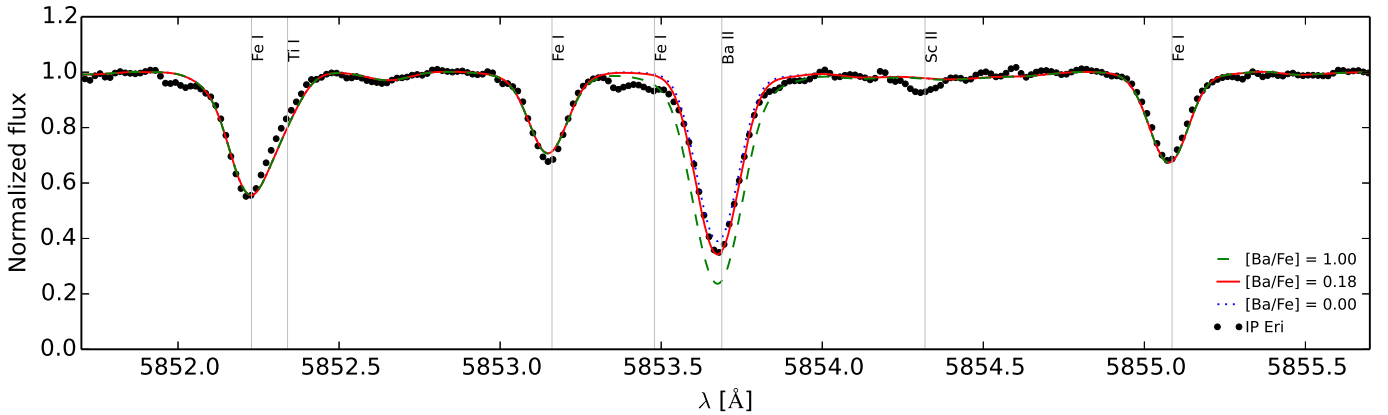


Fig. 5. Example of Ba II line fitting (Ba II λ 585.37 nm).

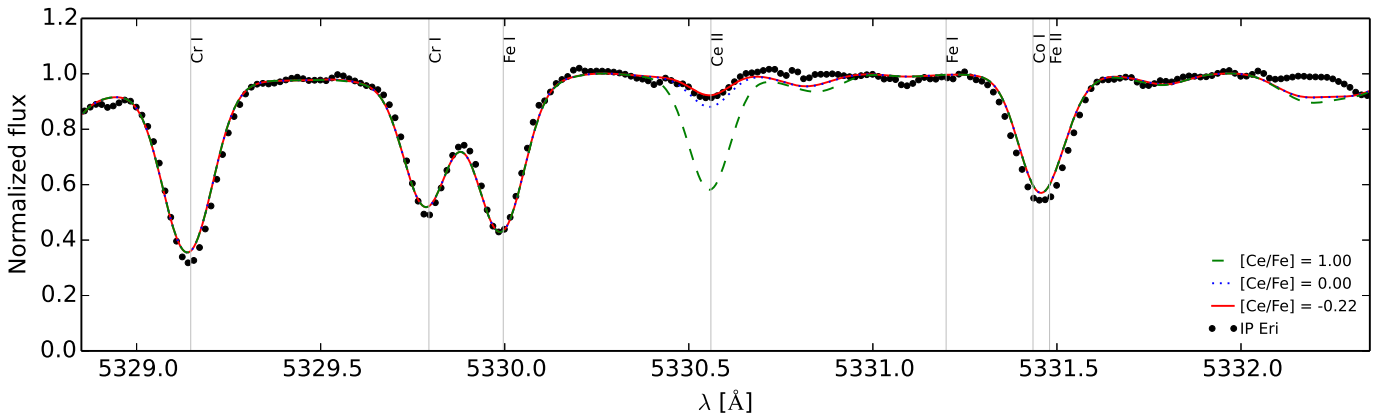


Fig. 6. Example of Ce II line fitting (Ce II λ 533.01 nm).

derived from ionized lines. This trend, if real, could be explained by the NLTE mechanism of overionization of the dominant neutral species due to UV radiation of non-local origin as shown, e.g., for Mg by Merle et al. (2011) or for Fe by Lind et al. (2012). These NLTE effects altering the ionization equilibrium of *s*-process elements should be investigated, but such an analysis is beyond the scope of this paper.

An average light-*s*-process abundance of $[ls/Fe] = 0.14 \pm 0.04$ is obtained, based on Sr I, Y II, and Zr II abundances, as compared to $[hs/Fe] = -0.03 \pm 0.05$, based on Ba II, La II, and Ce II abundances. The subsolar Ce II abundance is supported by a sim-

ilarly subsolar Nd abundance, as derived from Nd II lines. Thus, there does not seem to be a significant *s*-process enrichment in IP Eri. This issue is discussed further in Sect. 6, where the IP Eri abundances are confronted with abundances in barium stars and with expectations from the chemical evolution of the Galaxy.

6. Confrontation with normal field stars and barium stars

We have compared the abundances of IP Eri with those of field stars and with those from a sample of mild barium stars, to con-

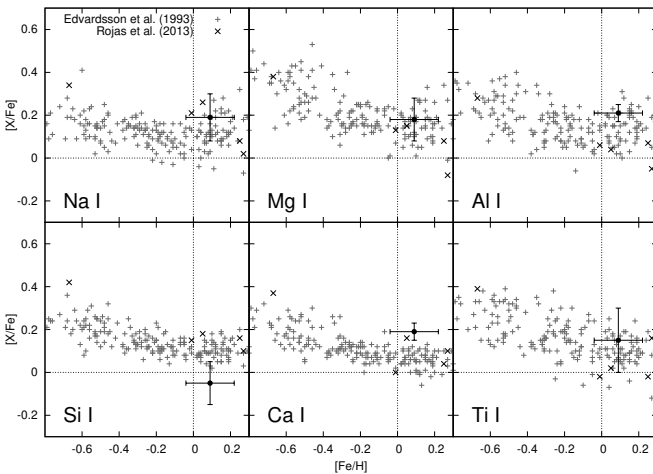


Fig. 7. Comparison of light-element abundances in IP Eri (black dot), in field stars (Edvardsson et al. 1993, grey plusses), and in mild barium stars (Rojas et al. 2013, black crosses).

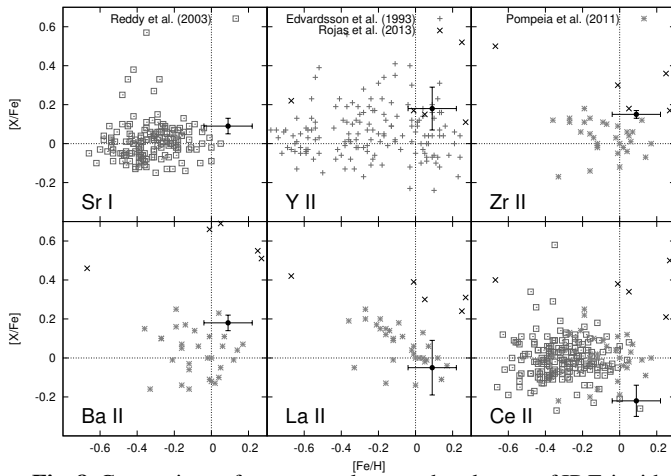


Fig. 8. Comparison of s-process element abundances of IP Eri with field stars (Edvardsson et al. 1993, grey plusses), (Reddy et al. 2003, grey squares), (Pompéia et al. 2011, grey asterisks) and mild barium stars (Rojas et al. 2013, black crosses).

firm that the abundances of *s*-process elements in IP Eri derived in Sect. 5.3 are by no means peculiar.

We first consider the light-element abundances [X/Fe] in IP Eri which are compared in Fig. 7 with abundances in a large sample of F and G stars from the galactic disc (Edvardsson et al. 1993). We corrected for the zero-point solar abundance offset, since Edvardsson et al. (1993) used a different reference value of $A_{\odot}(\text{Fe}) = 7.51$. Fig. 7 shows that the light-element abundances in IP Eri are in relatively good agreement with those of moderately metal-rich stars. The Na I, Mg I, Al I and Ti I abundances of IP Eri are located within the abundance distribution of the galactic sample. O I (not shown in Fig. 7) and Ca I are slightly more abundant as compared to the disc stars. The oxygen overabundance may be trusted though, since Edvardsson et al. (1993) used a scaling relation to transform abundances from the high excitation lines that they used ($\lambda 615.8 \text{ nm}$ as well as the $\lambda 777.3 \text{ nm}$ triplet) to the abundance from the [O I] $\lambda 630.0 \text{ nm}$ line that we used. For Ca, there are no lines in common with the Edvardsson et al. analysis. We used saturated and strong lines which are affected by NLTE effects, as shown by Mashonkina et al. (2007). These authors predict positive NLTE abundance corrections (between 0

and 0.07 dex for a model with $T_{\text{eff}} = 5000 \text{ K}$, $\log g = 3$ and $[\text{Fe}/\text{H}] = 0$), which, if accounted for, would further strengthen the Ca enrichment as compared to the Edvardsson et al. (1993) values for field stars. We have also compared IP Eri light-element abundances with those of a sample of mild barium stars from Rojas et al. (2013). Their light-element abundances are similar to those of field stars.

On the contrary, the Si I abundance of IP Eri (for which most of the lines used are common to the two studies) is lower than the value derived for the disc-star distribution. The IP Eri abundance of Ti I matches the average abundance of the disc stars of similar metallicities, but our value suffers from large error bars due to a larger set of lines in our analysis (9 against 4 for Edvardsson et al. 1993). This large dispersion may be partially explained by the fact that all the lines have equivalent widths larger than $150 \text{ m}\AA$ and are consequently less sensitive to abundance changes.

The *s*-process element abundances in IP Eri are compared with those of disc stars in Fig. 8. The comparison sample is from Edvardsson et al. (1993) for Y II, Reddy et al. (2003) for Sr I and Ce II, Pompéia et al. (2011) for Zr II, Ba II and La II. The slight enrichment in Y II, Zr II, and Ba II observed in IP Eri is typical of the enrichment trend observed for disc stars. Ce II appears peculiar in that it is underabundant in IP Eri as compared to disc stars of similar metallicities.

For Sr I, the only abundances available for comparison are from Reddy et al. (2003). They are based on a single line, and unfortunately, the Reddy et al. sample includes only stars with solar and sub-solar metallicities, giving the false impression that the IP Eri abundances are discrepant. For La II, data from Pompéia et al. (2011) are the only ones available for comparison, and the slight La II underabundance (with respect to the Sun) observed in IP Eri matches the trend observed among disc stars.

The comparison with the sample of mild barium stars of Rojas et al. (2013) is not discriminating for first-peak *s*-process elements (top panels of Fig. 8). But abundances from second-peak *s*-process elements in IP Eri are clearly lower than those of mild barium stars (bottom panels of Fig. 8). From these comparisons, we conclude that the slight enrichment in α and *s*-process elements in IP Eri is largely consistent with the chemical evolution of the Galaxy, so that there is no obvious signature from a chemical pollution resulting from mass transfer.

7. The evolutionary context of IP Eri

He WDs form when a star loses its hydrogen-rich envelope before it ignites helium. For a single star, this is not possible within a Hubble time since only stars with masses $M \lesssim 0.45 - 0.5 \text{ M}_{\odot}$ can avoid helium ignition. A binary scenario is therefore required.

As illustrated in Fig. 9, different evolutionary channels can account for these objects. The first one involves mass transfer by Roche lobe overflow (RLOF). The long period of IP Eri (1071 d) imposes that mass transfer starts while the star is already on the red-giant branch (late case B). Because of the presence of a deep convective envelope in the donor, two outcomes are possible depending on the mass ratio $q = M_{\text{donor}}/M_{\text{gainer}}$. If $q > 1.3 - 1.5$ (Soberman et al. 1997; Hurley et al. 2002), the mass transfer is dynamically unstable; after a rapid stage of common-envelope evolution, a short-period system forms (channel Ia in Fig. 9). In the alternative configuration ($q < 1.3 - 1.5$), soon after RLOF starts, the mass ratio reverses and subsequent mass transfer leads to the expansion of the orbit. The outcome is then a long-period

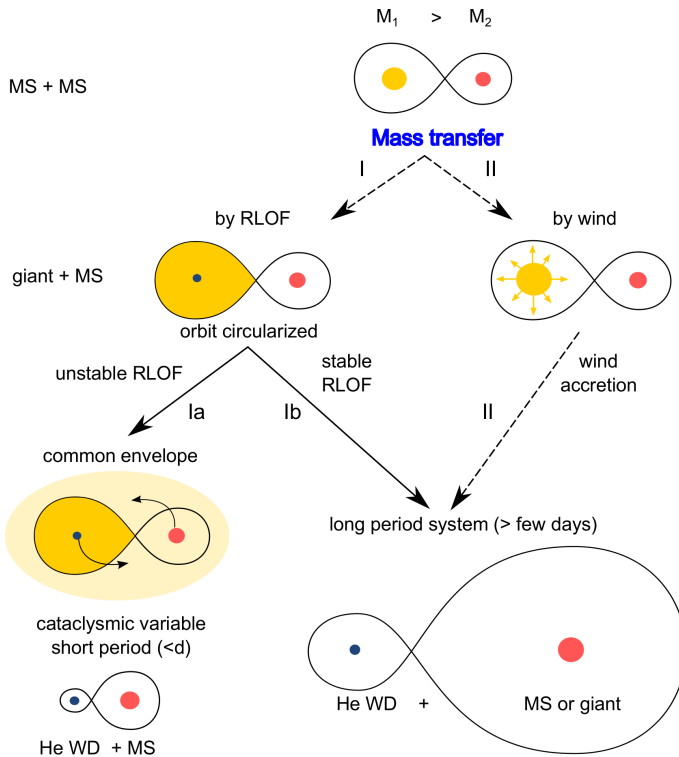


Fig. 9. Evolutionary channels for the formation of a He WD. The dashed lines refer to channels where the eccentricity can be preserved (see text for details).

system similar to IP Eri (channel Ib). However, in this RLOF scenario, tidal interactions are very strong because of the extended convective envelope of the Roche-filling donor star and the orbit always circularizes. This channel thus cannot explain the high eccentricity of IP Eri.

A solution to the eccentricity problem has been described in a companion paper (Siess et al. 2014). Based on binary-evolution calculations with the code BINSTAR (Siess et al. 2013; Davis et al. 2013; Deschamps et al. 2013), we showed that if the envelope of the He-WD progenitor is lost via tidally-enhanced winds (channel II), the circularization can be avoided. Tout & Eggleton (1988) suggested that the presence of a companion star can substantially increase the mass-loss rate of the evolved component. In this situation, the donor star loses its envelope while remaining inside its Roche potential and tidal forces are significantly reduced. Moreover, if the system has an initial eccentricity, the orbital wind mass-transfer modulation (Soker 2000) provides an eccentricity-pumping mechanism that counteracts the tidal circularization. We showed that such a scenario is able to account for all the orbital properties of a system like IP Eri.

In Fig. 10 we compare the orbital properties of IP Eri with those of pre- (K giants in open clusters from Mermilliod et al. 2007 and binary M giants from Famaey et al. 2009; Jorissen et al. 2009) and post-mass-transfer binaries (barium and S stars from Jorissen et al. 1998, updated with some recently published orbits from Gorlova et al. 2014). We also show in the $e - \log P$ diagram the location of the G5 IV + WD system HR 1608 ($= 63$ Eri). This system has an eccentricity ($e = 0.30 \pm 0.06$) and a period ($P = 903 \pm 5$ d) very similar to those of IP Eri (from Beavers & Eitter 1988, quoted by Landsman et al. 1993). The revised Hipparcos parallax (18.53 ± 0.84 mas; van Leeuwen 2007) yields a distance range 51 – 56 pc for HR 1608, which

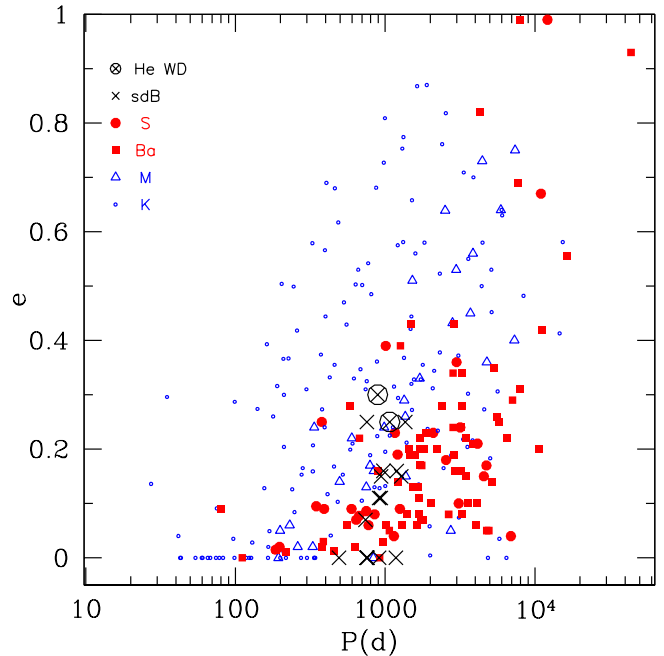


Fig. 10. The positions of IP Eri and its twin system HR 1608 (black circled crosses; Beavers & Eitter 1988, quoted by Landsman et al. 1993) in the eccentricity – period diagram are compared with those of the long-period sdB binaries, with (mostly) pre-mass-transfer binaries (normal K and M giants), and with post-mass-transfer binaries (Barium and S stars). Symbols are as indicated in the figure label.

implies a WD mass around $0.4 M_{\odot}$ (Landsman et al. 1993), and thus a He-WD. A more recent analysis of the WD parameters by Vennes et al. (1998) suggests instead a higher mass range ($0.51 - 0.67 M_{\odot}$). We also include in Fig. 10 the sdB binaries with long periods (black crosses) from Østensen & Van Winckel (2011, 2012), Vos et al. (2012, 2013), Deca et al. (2012), and Barlow et al. (2012, 2013).

IP Eri and HR 1608 have the largest eccentricities when compared to the long-period sdB systems, a fact whose significance is difficult to assess with so few He-WD systems. What seems significant, however, is the fact that (long-period) sdB and He-WD systems occupy a rather restricted period range around 10^3 d. In that respect, they differ from the barium and S binaries, two other families of post-mass-transfer systems, which spread over a more extended period range. This difference might be related to the fact that sdB and He-WD binaries are the end products of mass transfer occurring on the first red giant branch, whereas barium and S systems involved mass transfer on the AGB.

8. Summary

IP Eri is an unusual long-period binary system with a high eccentricity. Our abundance analysis reveals that it is not enriched in *s*-process elements, giving additional support to He-WD nature of the hot component that avoided evolution along the AGB. The abundances of the light elements do not reveal any peculiarities and within the error bars, the abundances are very close to solar. What is more surprising is that IP Eri alike its twin HR 1608 have the largest eccentricities among their closely related sdB systems and are very concentrated around a thousand-day period, which is likely related to the fact that the donor stars lose their envelope on the red-giant branch. However, the statistics

remains small and additional data are highly desirable in order to confirm the formation channel of these systems.

Acknowledgements. This work has been partly funded by an *Action de recherche concertée* (ARC) from the *Direction générale de l'Enseignement non obligatoire et de la Recherche scientifique – Direction de la recherche scientifique – Communauté française de Belgique*. T.M. is supported by the FNRS-F.R.S. as temporary post-doctoral researcher under grant No. 2.4513.11. The Mercator telescope is operated thanks to grant number G.0C31.13 of the FWO under the 'Big Science' initiative of the Flemish government. Based on observations obtained with the HERMES spectrograph, supported by the Fund for Scientific Research of Flanders (FWO), the Research Council of K.U.Leuven, the Fonds National de la Recherche Scientifique (F.R.S.-FNRS), Belgium, the Royal Observatory of Belgium, the Observatoire de Genève, Switzerland and the Thüringer Landessternwarte Tautenburg, Germany.

References

- Alvarez, R. & Plez, B. 1998, A&A, 330, 1109
 Asplund, M. 2005, ARA&A, 43, 481
 Bailer-Jones, C. A. L. 2011, MNRAS, 411, 435
 Barbuy, B., Jorissen, A., Rossi, S. C. F., & Arnould, M. 1992, A&A, 262, 216
 Barlow, B. N., Liss, S. E., Wade, R. A., & Green, E. M. 2013, ApJ, 771, 23
 Barlow, B. N., Wade, R. A., Liss, S. E., Østensen, R. H., & Van Winckel, H. 2012, ApJ, 758, 58
 Barstow, M. A., Bond, H. E., Burleigh, M. R., & Holberg, J. B. 2001, MNRAS, 322, 891
 Beavers, W. I. & Eitter, J. J. 1988, in Bulletin of the American Astronomical Society, Vol. 20, Bulletin of the American Astronomical Society, 737
 Bessell, M. S., Castelli, F., & Plez, B. 1998, A&A, 333, 231
 Bidelman, W. P. & Keenan, P. C. 1951, 114, 473
 Bowyer, S., Lampton, M., Lewis, J., et al. 1996, ApJS, 102, 129
 Bowyer, S., Lieu, R., Lampton, M., et al. 1994, ApJS, 93, 569
 Burleigh, M. R., Barstow, M. A., & Fleming, T. A. 1997, MNRAS, 287, 381
 Chubak, C., Marcy, G., Fischer, D. A., et al. 2012, ArXiv e-prints
 Cox, A. N. 2000, Allen's astrophysical quantities
 Cutispoto, G., Pallavicini, R., Kuerster, M., & Rodono, M. 1995, A&A, 297, 764
 Cutispoto, G., Pastori, L., Tagliaferri, G., Messina, S., & Pallavicini, R. 1999, A&AS, 138, 87
 Cutri, R. M., Skrutskie, M. F., van Dyk, S., et al. 2003, VizieR Online Data Catalog, 2246, 0
 Davis, P. J., Siess, L., & Deschamps, R. 2013, A&A, 556, A4
 Deca, J., Marsh, T. R., Østensen, R. H., et al. 2012, MNRAS, 421, 2798
 Deschamps, R., Siess, L., Davis, P. J., & Jorissen, A. 2013, A&A, 557, A40
 Drake, N. A. & Pereira, C. B. 2008, AJ, 135, 1070
 Driebe, T., Schoenberner, D., Bloecker, T., & Herwig, F. 1998, A&A, 339, 123
 Edvardsson, B., Andersen, J., Gustafsson, B., et al. 1993, A&A, 275, 101
 Famaey, B., Pourbaix, D., Frankowski, A., et al. 2009, A&A, 498, 627
 Gilmore, G., Randich, S., Asplund, M., et al. 2012, The Messenger, 147, 25
 Gorlova, N., Van Winckel, H., Vos, J., et al. 2014, A. Tkachenko (ed.), "Setting a new standard in the analysis of binary stars" EAS Conf. Ser., arXiv 1403.2287
 Grevesse, N., Asplund, M., & Sauval, A. J. 2007, Space Sci. Rev., 130, 105
 Gustafsson, B., Edvardsson, B., Eriksson, K., et al. 2008, A&A, 486, 951
 Heber, U. 2009, ARA&A, 47, 211
 Hurley, J. R., Pols, O. R., & Tout, C. A. 2000, MNRAS, 315, 543
 Hurley, J. R., Tout, C. A., & Pols, O. R. 2002, MNRAS, 329, 897
 Jofre, P., Heiter, U., Soubiran, C., et al. 2013, ArXiv e-prints
 Jorissen, A., Frankowski, A., Famaey, B., & van Eck, S. 2009, A&A, 498, 489
 Jorissen, A., Van Eck, S., Mayor, M., & Udry, S. 1998, A&A, 332, 877
 Kupka, F. G., Ryabchikova, T. A., Piskunov, N. E., Stempels, H. C., & Weiss, W. W. 2000, Baltic Astronomy, 9, 590
 Landsman, W., Simon, T., & Bergeron, P. 1993, PASP, 105, 841
 Lind, K., Bergemann, M., & Asplund, M. 2012, MNRAS, 427, 50
 Malina, R. F., Marshall, H. L., Antia, B., et al. 1994, AJ, 107, 751
 Mashonkina, L., Korn, A. J., & Przybilla, N. 2007, A&A, 461, 261
 Masseron, T. 2006, PhD thesis, Observatoire de Paris
 Masseron, T., Plez, B., Van Eck, S., et al. 2014, A&A, in press
 Merle, T., Thévenin, F., Pichon, B., & Bigot, L. 2011, MNRAS, 418, 863
 Mermilliod, J.-C., Andersen, J., Latham, D. W., & Mayor, M. 2007, A&A, 473, 829
 Østensen, R. H. & Van Winckel, H. 2011, in Astronomical Society of the Pacific Conference Series, Vol. 447, Evolution of Compact Binaries, ed. L. Schmidtobreck, M. R. Schreiber, & C. Tappert, 171
 Østensen, R. H. & Van Winckel, H. 2012, in Astronomical Society of the Pacific Conference Series, Vol. 452, Fifth Meeting on Hot Subdwarf Stars and Related Objects, ed. D. Kilkenny, C. S. Jeffery, & C. Koen, 163
 Plez, B. 2012, Astrophysics Source Code Library, 5004
 Pojmanski, G. 1997, Acta Astron., 47, 467
- Pompéia, L., Masseron, T., Famaey, B., et al. 2011, MNRAS, 415, 1138
 Pounds, K. A., Allan, D. J., Barber, C., et al. 1993, MNRAS, 260, 77
 Pye, J. P., McGale, P. A., Allan, D. J., et al. 1995, MNRAS, 274, 1165
 Raskin, G., van Winckel, H., Hensberge, H., et al. 2011, A&A, 526, A69
 Reddy, B. E., Tomkin, J., Lambert, D. L., & Allende Prieto, C. 2003, MNRAS, 340, 304
 Rojas, M., Drake, N. A., Pereira, C. B., & Kholygin, A. F. 2013, Astrophysics, 56, 57
 Siess, L., Davis, P. J., & Jorissen, A. 2014, A&A, in press
 Siess, L., Izzard, R. G., Davis, P. J., & Deschamps, R. 2013, A&A, 550, 100
 Soberman, G. E., Phinney, E. S., & van den Heuvel, E. P. J. 1997, A&A, 327, 620
 Soker, N. 2000, A&A, 357, 557
 Strassmeier, K., Washuettl, A., Granzer, T., Scheck, M., & Weber, M. 2000, A&AS, 142, 275
 Tout, C. A. & Eggleton, P. P. 1988, MNRAS, 231, 823
 Udry, S., Mayor, M., Maurice, E., et al. 1999a, in Astronomical Society of the Pacific Conference Series, Vol. 185, IAU Colloq. 170: Precise Stellar Radial Velocities, ed. J. B. Hearnshaw & C. D. Scarfe, 383
 Udry, S., Mayor, M., & Queloz, D. 1999b, in Astronomical Society of the Pacific Conference Series, Vol. 185, IAU Colloq. 170: Precise Stellar Radial Velocities, ed. J. B. Hearnshaw & C. D. Scarfe, 367
 van Leeuwen, F. 2007, A&A, 474, 653
 Vennes, S., Christian, D. J., Mathioudakis, M., & Doyle, J. G. 1997, A&A, 318, L9
 Vennes, S., Christian, D. J., & Thorstensen, J. R. 1998, ApJ, 502, 763
 Vennes, S., Mathioudakis, M., Doyle, J. G., Thorstensen, J. R., & Byrne, P. B. 1995, A&A, 299, L29
 Vos, J., Østensen, R. H., Degroote, P., et al. 2012, A&A, 548, A6
 Vos, J., Østensen, R. H., Németh, P., et al. 2013, A&A, 559, A54

Appendix A: Linelist

Table A.1. Line list used for determining atmospheric parameters and chemical composition of atomic species. The main source for oscillator strengths ($\log gf$) is VALD. Fitted individual absolute abundances $A(X)$ are also given. The absolute solar abundances $A_{\odot}(X)$ are from Grevesse et al. (2007). Vertical lines in the left margin mean that all transitions contribute to the same line (fine or hyperfine structure). For Ba II, the atomic mass of the contributing isotope is indicated as a superscript to the transition wavelength.

	λ [nm]	χ [eV]	$\log gf$	$A(X)$
C I		$A_{\odot}(\text{C}) = 8.39$		
493.2049	7.685	-1.884	8.25	
538.0337	7.685	-1.615	8.63	
555.3174	8.643	-2.370	8.45	
633.5701	8.771	-2.370	8.63	
633.7183	8.771	-2.450	8.65	
658.7610	8.537	-1.021	8.62	
661.1353	8.851	-1.837	8.64	
667.1845	8.851	-1.651	8.61	
768.5190	8.771	-1.519	8.58	
784.8241	8.848	-1.731	8.68	
785.2859	8.851	-1.683	8.74	
786.0877	8.851	-1.148	8.65	
788.4490	8.847	-1.580	8.31	
807.8479	8.848	-1.817	8.69	
833.5148	7.685	-0.420	8.60	
872.7126	1.264	-8.136	8.61	
881.8479	9.003	-1.060	8.20	
N I		$A_{\odot}(\text{N}) = 7.78$		
868.3403	10.330	0.086	7.85	
O I		$A_{\odot}(\text{O}) = 8.66$		
630.0304	0.000	-9.715	8.82	
Na I		$A_{\odot}(\text{Na}) = 6.17$		
449.7657	2.104	-1.560	6.36	
498.2814	2.104	-0.950	6.38	
568.2633	2.102	-0.706	6.25	
568.8205	2.104	-0.450	6.45	
615.4226	2.102	-1.547	6.53	
616.0747	2.104	-1.246	6.48	
818.3255	2.102	0.230	6.60	
819.4824	2.104	0.490	6.54	
Mg I		$A_{\odot}(\text{Mg}) = 7.53$		
552.8405	4.346	-0.620	7.70	
571.1088	4.346	-1.833	7.67	
631.8717	5.108	-2.103	7.86	
631.9237	5.108	-2.324	7.92	
631.9495	5.108	-2.803	7.89	
738.7689	5.753	-1.100	7.82	
769.1553	5.753	-0.783	7.68	
871.2676	5.932	-1.670	7.80	
871.2689	5.932	-1.370		
871.7825	5.933	-0.930	7.75	
873.6019	5.946	-0.690	7.96	
873.6029	5.946	-1.020		
Al I		$A_{\odot}(\text{Al}) = 6.37$		
555.7063	6.143	-2.104	6.63	
669.6023	3.143	-1.569	6.69	
669.8673	3.143	-1.870	6.73	
783.5309	4.022	-0.649	6.68	
783.6134	4.022	-0.494	6.71	
877.2865	4.022	-0.170	6.64	
877.3896	4.022	-0.161	6.75	
Si I		$A_{\odot}(\text{Si}) = 7.51$		
566.5555	4.920	-1.940	7.31	
568.4484	4.954	-1.553	7.55	

Table A.1. Continued.

λ [nm]	χ [eV]	$\log gf$	$A(X)$
569.0425	4.930	-1.773	7.50
570.1104	4.930	-1.953	7.57
577.2146	5.082	-1.653	7.64
579.3073	4.930	-1.963	7.62
612.5021	5.614	-1.464	7.60
613.1573	5.616	-1.556	7.52
613.1852	5.616	-1.615	7.57
614.2483	5.619	-1.295	7.43
614.5016	5.616	-1.310	7.54
615.5134	5.619	-0.754	7.70
624.4466	5.616	-1.093	7.42
776.0628	6.206	-1.261	7.65
872.8010	6.181	-0.370	7.61
Ca I			
558.8749	2.526	0.358	6.62
585.7451	2.933	0.240	6.50
610.2723	1.879	-0.793	6.60
612.2217	1.886	-0.316	6.59
616.2173	1.899	-0.090	6.61
643.9075	2.526	0.390	6.55
649.3781	2.521	-0.109	6.57
649.9650	2.523	-0.818	6.64
Ti I			
453.4776	0.836	0.280	5.31
454.8763	0.826	-0.354	4.99
498.1731	0.848	0.560	5.18
499.9503	0.826	0.306	5.24
502.4844	0.818	-0.546	5.05
503.9957	0.021	-1.074	5.02
517.3743	0.000	-1.062	4.97
519.2969	0.021	-1.006	5.39
521.0385	0.048	-0.527	5.09
Ti II			
453.3960	1.237	-0.530	4.86
456.3757	1.221	-0.690	5.05
457.1968	1.572	-0.320	4.99
533.6771	1.582	-1.630	4.98
538.1015	1.566	-1.970	5.26
Fe I			
480.8148	3.251	-2.690	7.58
496.2572	4.178	-1.182	7.48
499.2785	4.260	-2.350	7.71
505.8496	3.642	-2.830	7.73
524.3776	4.256	-1.050	7.51
525.3021	2.279	-3.840	7.50
529.4547	3.640	-2.760	7.62
529.5312	4.415	-1.590	7.55
537.3709	4.473	-0.760	7.45
537.9574	3.694	-1.514	7.48
538.9479	4.415	-0.410	7.24
539.7618	3.634	-2.528	7.68
539.8279	4.445	-0.630	7.65
541.2784	4.434	-1.716	7.41
541.7033	4.415	-1.580	7.43
543.6295	4.386	-1.440	7.65
544.1339	4.312	-1.630	7.36
546.6396	4.371	-0.630	7.62
547.3163	4.191	-2.040	7.53
548.3099	4.154	-1.406	7.57
548.7145	4.415	-1.430	7.43
549.1832	4.186	-2.188	7.51
549.4463	4.076	-1.990	7.54
552.2446	4.209	-1.450	7.47
553.9280	3.642	-2.560	7.22
554.3936	4.217	-1.040	7.36
554.9949	3.694	-2.810	7.50
556.0212	4.434	-1.090	7.50
557.7025	5.033	-1.543	7.69
561.8632	4.209	-1.275	7.46
563.3946	4.991	-0.230	7.38
563.8262	4.220	-0.770	7.63

Table A.1. Continued.

λ [nm]	χ [eV]	$\log gf$	$A(X)$
565.1469	4.473	-1.900	7.75
565.2318	4.260	-1.850	7.68
566.1345	4.284	-1.756	7.52
567.9023	4.652	-0.820	7.53
570.5464	4.301	-1.355	7.46
573.1762	4.256	-1.200	7.66
573.2296	4.991	-1.460	7.67
574.1848	4.256	-1.672	7.57
575.2032	4.549	-1.177	7.78
577.5081	4.220	-1.297	7.75
577.8453	2.588	-3.430	7.46
584.9683	3.694	-2.890	7.57
585.5076	4.608	-1.478	7.49
585.8778	4.220	-2.160	7.49
586.1109	4.283	-2.304	7.44
590.5671	4.652	-0.690	7.25
592.7789	4.652	-0.990	7.41
593.0180	4.652	-0.230	7.70
593.4655	3.928	-1.070	7.50
595.6694	0.859	-4.553	7.54
602.7051	4.076	-1.089	7.46
605.6005	4.733	-0.460	7.58
609.3643	4.607	-1.400	7.62
615.1617	2.176	-3.312	7.54
616.5360	4.143	-1.473	7.48
617.3334	2.223	-2.880	7.64
618.7989	3.943	-1.620	7.50
620.0313	2.608	-2.405	7.72
622.6734	3.883	-2.120	7.59
627.0223	2.858	-2.536	7.43
632.2685	2.588	-2.448	7.74
643.6406	4.186	-2.580	7.80
647.5624	2.559	-2.941	7.79
648.1870	2.279	-2.985	7.57
649.8938	0.958	-4.688	7.48
651.8366	2.831	-2.373	7.36
665.3851	4.154	-2.215	7.42
669.9141	4.593	-2.101	7.53
671.0318	1.485	-4.764	7.48
671.3743	4.795	-1.500	7.69
672.5356	4.103	-2.013	7.42
672.6666	4.607	-1.133	7.67
673.9521	1.557	-4.794	7.46
675.0152	2.424	-2.604	7.69
681.0262	4.607	-0.986	7.55
848.1981	4.186	-1.988	7.51
851.5108	3.018	-2.073	7.72
852.7852	5.020	-1.625	7.73
857.1804	5.010	-1.414	7.91
859.8829	4.386	-1.088	7.49
862.1601	2.949	-2.320	7.67
863.2414	4.103	-2.341	7.53
869.8706	2.990	-3.452	7.74
869.9454	4.955	-0.380	7.51
880.4623	2.279	-3.234	7.66
Fe II			
499.3358	2.807	-3.684	7.32
523.4625	3.221	-2.180	7.60
525.6938	2.891	-4.182	7.64
532.5553	3.221	-3.160	7.44
533.7732	3.230	-3.720	7.63
541.4073	3.221	-3.580	7.35
542.5257	3.199	-3.220	7.29
553.4847	3.245	-2.865	7.48
599.1376	3.153	-3.647	7.63
608.4111	3.199	-3.881	7.59
611.3322	3.221	-4.230	7.59
614.9258	3.889	-2.841	7.66
624.7557	3.892	-2.435	7.52
636.9462	2.891	-4.110	7.44
643.2680	2.891	-3.570	7.54
645.6383	3.903	-2.185	7.71
Sr I	$A_{\odot}(\text{Sr}) = 2.92$		
483.2108	1.798	-0.110	3.11

Table A.1. Continued.

λ [nm]	χ [eV]	$\log gf$	$A(X)$
496.2259	1.847	0.200	3.06
707.0070	1.847	-0.030	3.13
Y I			$A_{\odot}(Y) = 2.21$
619.1718	0.000	-0.970	2.38
643.5004	0.066	-0.820	2.28
Y II			
490.0120	1.033	0.103	1.84
520.0406	0.992	-0.570	2.01
520.5724	1.033	-0.193	2.00
528.9815	1.033	-1.850	2.03
679.5414	1.738	-1.030	1.80
Zr I			$A_{\odot}(Zr) = 2.58$
482.8041	0.623	-0.640	2.81
612.7475	0.154	-1.060	2.82
613.4585	0.000	-1.280	2.76
807.0115	0.730	-0.790	3.16
Zr II			
444.2992	1.486	-0.420	2.82
535.0089	1.827	-1.240	2.81
Ba II			$A_{\odot}(Ba) = 2.17$
455.3998 ¹³⁷	0.000	-0.666	
455.3999 ¹³⁷	0.000	-0.666	
455.4000 ¹³⁷	0.000	-1.064	
455.4001 ¹³⁵	0.000	-0.666	
455.4002 ¹³⁵	0.000	-1.064	
455.4002 ¹³⁵	0.000	-0.666	
455.4031 ¹³⁰	0.000	0.140	
455.4031 ¹³²	0.000	0.140	
455.4031 ¹³⁴	0.000	0.140	2.42
455.4032 ¹³⁶	0.000	0.140	
455.4033 ¹³⁸	0.000	0.140	
455.4048 ¹³⁵	0.000	-0.219	
455.4050 ¹³⁵	0.000	-0.666	
455.4051 ¹³⁷	0.000	-0.219	
455.4052 ¹³⁵	0.000	-1.365	
455.4054 ¹³⁷	0.000	-0.666	
455.4055 ¹³⁷	0.000	-1.365	
585.3669 ¹³⁵	0.604	-1.967	
585.3669 ¹³⁷	0.604	-1.967	
585.3670 ¹³⁵	0.604	-2.113	
585.3670 ¹³⁵	0.604	-1.909	
585.3671 ¹³⁷	0.604	-2.113	
585.3671 ¹³⁷	0.604	-1.909	
585.3672 ¹³⁵	0.604	-2.113	
585.3672 ¹³⁵	0.604	-2.511	
585.3673 ¹³⁰	0.604	-0.909	
585.3673 ¹³²	0.604	-0.909	
585.3673 ¹³⁴	0.604	-0.909	
585.3673 ¹³⁷	0.604	-2.113	2.43
585.3673 ¹³⁵	0.604	-1.812	
585.3673 ¹³⁷	0.604	-2.511	
585.3674 ¹³⁶	0.604	-0.909	
585.3675 ¹³⁵	0.604	-1.909	
585.3675 ¹³⁵	0.604	-1.365	
585.3675 ¹³⁷	0.604	-1.812	
585.3675 ¹³⁸	0.604	-0.909	
585.3676 ¹³⁷	0.604	-1.909	
585.3676 ¹³⁷	0.604	-1.365	
585.3680 ¹³⁵	0.604	-1.967	
585.3682 ¹³⁷	0.604	-1.967	
614.1708 ¹³⁵	0.704	-0.456	
614.1708 ¹³⁵	0.704	-1.264	
614.1709 ¹³⁵	0.704	-2.410	
614.1709 ¹³⁷	0.704	-1.264	
614.1709 ¹³⁷	0.704	-0.456	

Table A.1. Continued.

λ [nm]	χ [eV]	$\log gf$	$A(X)$
614.1710 ¹³⁷	0.704	-2.410	
614.1711 ¹³⁰	0.704	-0.030	
614.1711 ¹³²	0.704	-0.030	
614.1711 ¹³⁴	0.704	-0.030	
614.1712 ¹³⁶	0.704	-0.030	
614.1713 ¹³⁵	0.704	-0.662	
614.1713 ¹³⁸	0.704	-0.030	2.40
614.1714 ¹³⁵	0.704	-1.167	
614.1715 ¹³⁵	0.704	-2.234	
614.1715 ¹³⁷	0.704	-0.662	
614.1716 ¹³⁵	0.704	-0.912	
614.1716 ¹³⁷	0.704	-1.167	
614.1717 ¹³⁵	0.704	-1.234	
614.1717 ¹³⁵	0.704	-1.280	
614.1717 ¹³⁷	0.704	-2.234	
614.1718 ¹³⁷	0.704	-0.912	
614.1719 ¹³⁷	0.704	-1.234	
614.1719 ¹³⁷	0.704	-1.280	
6496.883 ¹³⁵	0.604	-1.911	
6496.883 ¹³⁷	0.604	-1.911	
6496.888 ¹³⁵	0.604	-1.212	
6496.888 ¹³⁷	0.604	-1.212	
6496.895 ¹³⁰	0.604	-0.406	
6496.895 ¹³²	0.604	-0.406	
6496.895 ¹³⁴	0.604	-0.406	
6496.895 ¹³⁵	0.604	-0.765	
6496.896 ¹³⁷	0.604	-0.765	2.49
6496.897 ¹³⁶	0.604	-0.406	
6496.898 ¹³⁸	0.604	-0.406	
6496.900 ¹³⁵	0.604	-1.610	
6496.902 ¹³⁵	0.604	-1.212	
6496.902 ¹³⁷	0.604	-1.610	
6496.904 ¹³⁷	0.604	-1.212	
6496.906 ¹³⁵	0.604	-1.212	
6496.909 ¹³⁷	0.604	-1.212	
La II		$A_{\odot}(\text{La}) = 1.13$	
408.6695	0.000	-1.266	
408.6699	0.000	-1.108	
408.6702	0.000	-1.119	
408.6705	0.000	-1.292	
408.6708	0.000	-0.696	
408.6709	0.000	-1.094	
408.6710	0.000	-1.790	1.04
408.6711	0.000	-1.468	
408.6711	0.000	-3.216	
408.6717	0.000	-1.292	
408.6719	0.000	-1.119	
408.6720	0.000	-1.108	
408.6721	0.000	-1.266	
455.8457	0.321	-0.970	1.15
457.4860	0.173	-1.08	1.24
492.0965	0.126	-2.261	
492.0965	0.126	-2.407	
492.0966	0.126	-2.065	
492.0966	0.126	-2.078	
492.0966	0.126	-2.738	
492.0968	0.126	-1.831	
492.0968	0.126	-1.956	
492.0968	0.126	-2.629	
492.0971	0.126	-1.646	
492.0971	0.126	-1.895	1.32
492.0971	0.126	-2.650	
492.0975	0.126	-1.490	
492.0975	0.126	-1.891	
492.0975	0.126	-2.760	
492.0979	0.126	-1.354	
492.0979	0.126	-1.957	
492.0979	0.126	-2.972	
492.0985	0.126	-1.233	

Table A.1. Continued.

λ [nm]	χ [eV]	$\log gf$	$A(X)$
492.0985	0.126	-2.162	
492.0985	0.126	-3.375	
530.3513	0.321	-1.874	
530.3513	0.321	-2.363	
530.3514	0.321	-3.062	
530.3531	0.321	-2.167	
530.3532	0.321	-2.247	1.32
530.3532	0.321	-2.622	
530.3546	0.321	-2.366	
530.3546	0.321	-2.622	
530.3547	0.321	-2.351	
579.7565	0.244	-1.360	1.33
588.0633	0.235	-1.830	1.11
632.0376	0.173	-1.520	1.04
639.0455	0.321	-2.012	
639.0468	0.321	-2.183	
639.0468	0.321	-2.752	
639.0479	0.321	-2.570	
639.0479	0.321	-3.752	
639.0480	0.321	-2.390	
639.0489	0.321	-2.536	
639.0489	0.321	-3.334	1.23
639.0490	0.321	-2.661	
639.0496	0.321	-3.100	
639.0497	0.321	-2.595	
639.0498	0.321	-3.079	
639.0502	0.321	-2.954	
639.0503	0.321	-2.778	
639.0506	0.321	-2.857	
677.4268	0.126	-1.708	0.92
Ce II	$A_{\odot}(\text{Ce}) = 1.70$		
407.3374	0.478	0.230	1.52
452.3075	0.516	-0.030	1.54
456.2359	0.478	0.230	1.54
533.0556	0.869	-0.400	1.68
Nd II	$A_{\odot}(\text{Nd}) = 1.45$		
402.1327	0.321	-0.100	1.35
405.9950	0.205	-0.520	1.59
464.5760	0.559	-0.760	1.50
485.9026	0.321	-0.440	1.59
495.9115	0.064	-0.800	1.62
523.4190	0.550	-0.510	1.56
527.6869	0.859	-0.440	1.30
531.9810	0.550	-0.140	1.52